Yuxin Hu
yuxinh@stanford.edu

Comparison of shot-LLR and MUSSELS for multi-shot diffusion-weighted image reconstruction

1. Introduction

As a non-invasive imaging method, diffusion-weighted MRI has been widely used in clinical applications (1, 2) and neuroscientific research (3, 4). Single-shot echo planar imaging (EPI) is the most commonly used method because of its fast acquisition speed and immunity to motion. It is, however, limited by image blurring and distortion due to the long readout window (5). Multi-shot EPI has been shown to provide high-resolution diffusion-weighted images (DWIs) with reduced distortion (5). Unfortunately, significant aliasing artifacts and signal cancellation exist due to the mismatch of the motion-induced phase between different shots (5). The reconstruction becomes non-convex and intractable to solve when this phase is included in the forward model.

Many methods have been developed to estimate the motion-induced phase, either by navigator (6, 8) or parallel imaging (9-11). Unfortunately, acquisition of navigator data increases scan time and there might be a mismatch between the extra-navigator and the data to be reconstructed. Parallel imaging based on phase estimation methods might fail in case of high-frequency phase variations due to large motion.

We have proposed a locally low-rank reconstruction approach to reconstruct multi-shot DWIs, named shot-LLR. This method bypasses the challenging phase estimation step by using a relaxed model. We also notice several papers have been published to solve the phase mismatch problem by forming a block-Hankel matrix in k-space domain, called MUSSELS (12). In this work, we want to evaluate the performance of these two methods in vivo.

2. Theory

The formulation of shot-LLR and MUSSELS mirror CLEAR (13) and SAKE (14), respectively, which are two kinds of calibration-less image reconstruction methods. Interestingly, to the best of my knowledge, no comparison between SAKE and CLEAR has been done. In this section, we will introduce CLEAR and SAKE first, then shot-LLR and MUSSELS.

2.1 CLEAR

The formulation of CLEAR is

$$P1: \min_{x_{1,\ldots,N_C}} \sum_{i=1}^{N_C} \|DFx_i - y_i\|_2^2 + \lambda \sum_{b \in \Omega} \left\| R_b\{x_{1,\ldots,N_C}\} \right\|_* \quad (1)$$

where Nc is the number of coils, x_i and y_i are the images to be reconstructed, acquired data of the i^{th} coil, D is the sampling operator, F is Fourier transform, and λ is a regularization parameter. The first term is known as data fidelity term or data consistency term, no sensitivity information is needed here, and images of all coils will be reconstructed. The second term is a constraint on these images. This constraint is based on the assumption that sensitivity map is spatially smooth. We define an operator R_b, which extracts one small block at pixel index b in the image domain, reshapes it into a vector, and concatenates vectors from all shots into one matrix. With n pixels in one block, and N_C coils, an n-by-N_C spatial-coil matrix is constructed, in which $R_b\{x_{1,\ldots,N_C}\}_{i,j}$ represents the image at the i^{th} pixel and j^{th} shot. The spatial-coil matrix can be decomposed into the product of two matrices (Eq. 2).

$$R_b\{x_{1,\ldots,N_C}\} = \underbrace{\begin{bmatrix} I_1 & \cdots & 0 \\ \vdots & \ddots & \vdots \\ 0 & \cdots & I_n \end{bmatrix}}_{\mathrm{I}} \underbrace{\begin{bmatrix} S_{1,1} & \cdots & S_{1,N_C} \\ \vdots & \ddots & \vdots \\ S_{n,1} & \cdots & S_{n,N_C} \end{bmatrix}}_{S} \quad (3)$$

Each element of the diagonal matrix I represents the target image, and matrix S contains the sensitivity encoding information. If the sensitivity map is spatially smooth, then the rank of S would be low. Thus, the production of S and I would have a low rank. Ω is the set of all non-overlapping blocks which uniformly tile the image domain. In addition, the nuclear norm instead of rank is used to make the optimization problem convex and easy to solve.

2.2 SAKE

Different from CLEAR which constructs lots of small spatial-coil matrices, one block-Hankel matrix A is constructed with all k-space data in SAKE as in Fig 1. This construction is similar to R_b in CLEAR except two differences, (1) it is in k-space, and (2) each time, the block is shifted by only 1 pixel to make better use of the data, while in CLEAR these blocks are non-overlapped. It is proven that rank(A) ≤ $(w + s - 1)^2$, where w is the chosen window size and s is the coil sensitivity bandwidth in k-space (14). If the sensitivity is band limited in k-space which is equivalent to say that it is spatially smooth, then A is rank-deficient. Then similar to CLEAR, we can add a constraint on the rank of A, and the formulation is as follows,

$$P2: \min_{z_{1,\dots,N_C}} \sum_{i=1}^{N_s} \|Dz_i - y_i\|_2^2 + \lambda \left\| H\{z_{1,\dots,N_C}\} \right\|_* \quad (3)$$

where z_i is the k-space to be reconstructed of the i^{th} coil, H represents the operation to construct matrix A, and other parameters are defined the same as in CLEAR.

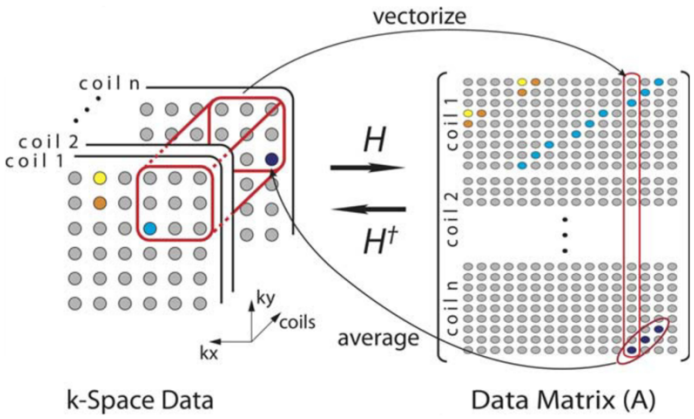

Fig 1. Construction of block-Hankel matrix with k-space from all coils (14).

2.3 Shot-LLR

In multi-shot DWI, different shots differ by a spatially smooth phase. Similar to calibration-less parallel imaging, we can also use locally low-rank regularization to reconstruct multi-shot DWIs. Different from CLEAR, sensitivity information is needed, and it is used to combine multi-channel images within one shot before forming the low-rank matrices, and the difference between different coil combined images comes from the motion-induced phase instead of sensitivity encoding. We formulate the reconstruction as the following optimization problem,

$$P3: \min_{x_{1,\dots,N_S}} \sum_{i=1}^{N_s} \|D_i F S x_i - y_i\|_2^2 + \lambda \sum_{b \in \Omega} \left\| R_b\{x_{1,\dots,N_S}\} \right\|_* \quad (4)$$

where N_s is the number of shots, D_i and x_i are sampling operator and images to be reconstructed of the i^{th} shot, S represents sensitivity encoding. Using the same operator R_b as in CLEAR, we can construct spatial-shot LLR matrix from images of all shots as shown in Fig 2., and this matrix can be decomposed into the product of two matrices (Eq. 5). Each element of diagonal matrix I represents the target complex image without motion-induced phase. Matrix

φ contains the motion-induced phase θ of each shot.

$$R_b\{x_{1,\dots,N_S}\} = \underbrace{\begin{bmatrix} I_1 & \cdots & 0 \\ \vdots & \ddots & \vdots \\ 0 & \cdots & I_n \end{bmatrix}}_{\mathrm{I}} \underbrace{\begin{bmatrix} e^{i\theta_{1,1}} & \cdots & e^{i\theta_{1,N_S}} \\ \vdots & \ddots & \vdots \\ e^{i\theta_{n,1}} & \cdots & e^{i\theta_{n,N_S}} \end{bmatrix}}_{\varphi} \quad (5)$$

If the motion-induced phase θ is spatially smooth, the rank of matrix φ is low. Consequently, $R_b\{x_{1,\dots,N_S}\}$ is also a low rank matrix. Intuitively, we can combine parallel imaging with a constraint on the rank of $R_b\{x_{1,\dots,N_S}\}$.

It should be noticed that because we parameterize the image by multiple images rather than motion-induced phase and one single image, no phase estimation is needed.

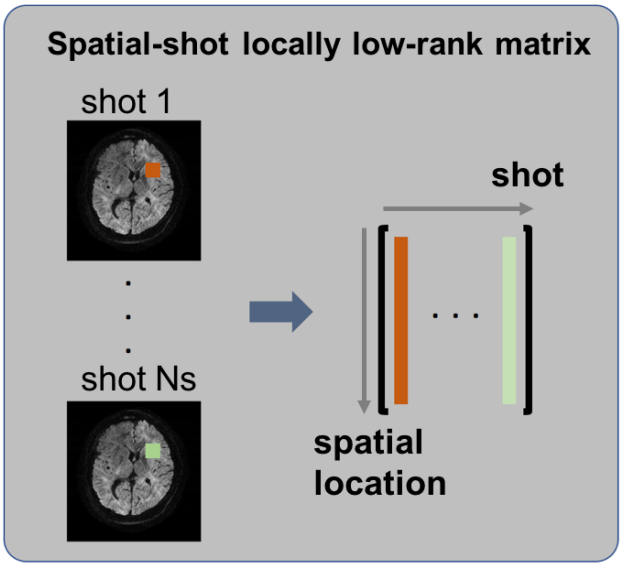

Fig. 2. Construction of the "spatial-shot" matrix containing a block of pixels from each of the shots. Because the motion-induced phase is slowly varying in the image domain, the spatial-shot matrices are low-rank. Therefore, constraints on the rank of these matrices can be used to remove the phase inconsistency.

2.4 MUSSELS

MUSSELS can be viewed as an extension of SAKE for multi-shot DWI reconstruction. Similar to shot-LLR, sensitivity information is included in the forward model to do coil combination before forming the block-Hankel matrix. The formulation is as follows:

$$P4: \min_{z_{1,\dots,N_S}} \sum_{i=1}^{N_S} \|D_i F S F^H z_i - y_i\|_2^2 + \lambda \left\| H\{z_{1,\dots,N_S}\} \right\|_* \quad (6)$$

Where z_i is the k-space to be reconstructed of the i^{th} shot, F^H represents inverse Fourier transform and other variables are defined the same as before. The first term is data consistency term and the second term is the constraint on the rank of the block-Hankel matrix. This matrix is constructed with the coil-combined k-space data of each shot. Since the motion-induced phase are spatially smooth, they are also band limited in k-space, and this matrix will be rank-deficient.

3. Methods

3.1 Simulation (CLEAR vs SAKE)

Since there is no gold standard for multi-shot DWI and it is hard to simulate the motion-induced phase, instead of comparing shot-LLR and MUSSELS, we compared SAKE and CLEAR to evaluate the influence of different constraints. We retrospectively under-sampled Shepp-Logan phantom data and brain data with different sampling patterns and reduction factors, and calculated the root-mean-square error (RMSE) and structural similarity (SSIM) of the reconstructed results compared with the fully sampled data.

3.2 In-vivo data (shot-LLR vs MUSSELS)

With approval from the institutional review board and written informed consent, brain, breast, and pelvis data were acquired on a 3 Tesla (T) MRI system (Discovery MR750, GE Healthcare) using a 2D single-refocused Stejskal-Tanner diffusion-weighted spin-echo EPI sequence.

The scan parameters are shown in Table 1. Bandwidth was set to 250 kHz, and partial Fourier acquisition was on for all experiments. Each time one non-diffusion-weighted image was acquired first, then diffusion-weighted data were acquired. In experiment (3), the volunteer was asked to breathe deeply to simulate severe respiratory motion.

3.3 Image reconstruction and implementation

CLEAR and shot-LLR were implemented based on the open-source Berkeley Advanced Reconstruction Toolbox (BART) with a block size of 8 × 8 (15). The optimization was solved using an iterative thresholding algorithm (FISTA). SAKE was implemented as original paper in Matlab using the projection onto convex sets (POCS) algorithm. MUSSELS was implemented based on SAKE.

POCS-MUSE, which is a commonly used multi-shot DWI reconstruction method, was also implemented for comparison. The number of iterations is 200 for all methods. Sensitivity maps were calculated from the multi-shot non-diffusion-weighted data by ESPIRiT (16). Homodyne was used for partial Fourier reconstruction (17).

Table 1. Scan parameters of all experiments.

Experiments	In-plane resolution (mm^2)	Slice thickness (mm)	Matrix size	b-value (s/mm^2)	Comments
(1) 4-shot brain	0.85 × 0.85	3	248 × 244	1000	--
(2) 8-shot brain			248 × 232		--
(3) 4-shot brain			248 × 244		severe motion
(4) 8-shot breast	1 × 1	4	360 × 360	600	no breath hold
(5) 4-shot pelvis	1.1 × 1.1	4	254 × 256	500	no breath hold

4. Results and Discussion

4.1 Simulation (CLEAR vs SAKE)

CLEAR and SAKE show pretty similar performance on these three different patterns as in Fig. 1: neither of them works on uniform under-sampled data, they work on Poisson-disc under-sampled data with some ACS lines, and they both work pretty well on variable density under-sampled data (up to a reduction factor of 7). We also evaluate the performance of these two methods on the Shepp-Logan phantom with simulated sensitivity map, and the same conclusion can be drawn.

We have checked the values of the constraint used for SAKE on the under-sampled data, and fully-sampled data. Surprisingly, uniformly under-sampled data has a lower value (not sure why? maybe because there are many zeros in it). But the singular values of the block-Hankel matrix from the fully-sampled data are more centralized. This suggests that **sum of these**

singular values may be not a good constraint for uniformly under-sampled data, and how these values are allocated may be more important.

4.2 In-vivo data (shot-LLR vs MUSSELS)

For brain DWI, shot-LLR and MUSSELS provide comparable image quality to POCS-MUSE for 4-shot acquisitions (Fig. 4.1) and markedly reduced aliasing artifact in comparison to POCS-MUSE for 8-shot acquisitions (Fig. 4.2). For 8-shot brain data, results of shot-LLR start to have some regions of signal loss (indicated by a white box in Fig. 4.2b), and results of MUSSELS have an un-expected dark region (highlighted by a yellow triangle in Fig. 4.2c) in comparison to 4-shot results. The reason for these artifacts is that these two methods both treat each shot as a separate image, and if some shot doesn't have central k-space data, then the recovery of that shot may fail, and this can even influence the reconstruction of other shots. For EPI, when the number of shots is high, there are always some shots which don't have central k-space lines. **Using variable density sampling patterns, e.g. variable density spiral and FSE, helps solve this problem**, but this is beyond the scope of this work.

When the volunteer breathed heavily, these two methods (Fig. 4.3b and 4.3c) are still very robust and there is no ghost artifact compared with POCS-MUSE (Fig. 4.3a). Interestingly, for breast and pelvis imaging, which are more susceptible to motion artifacts due to the proximity to the lungs and heart, severe aliasing artifacts are shown in MUSSELS (Fig. 5.1c and 5.2c), and shot-LLR has significantly fewer artifacts (Fig. 5.1b and 5.2b). By forming only one block-Hankel matrix in k-space, MUSSELS may utilize the inner-shot and inter-shot relationships better as shown in 8-shot brain DWI (Fig 4.3c). While shot-LLR has the capability to handle more complicated phase variations in body imaging (Fig 5.1 and 5.2). This motion robustness property of shot-LLR benefits from the fact that **the constraint is on the sum of the ranks in shot-LLR, some blocks can still have high-frequency phase variations.**

(1) Uniform sampling, R = 2

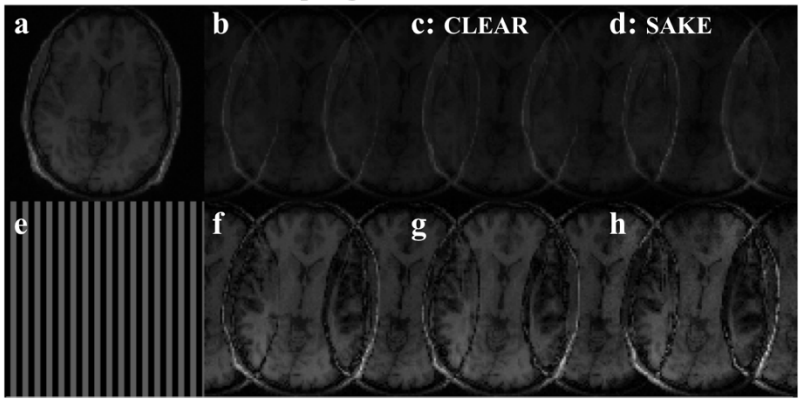

SSIM	0.5288	0.5250	0.5272
RMSE	0.1621	0.1627	0.1665

(2) Poisson-disc sampling, R = 2.7 with 10 ACS lines

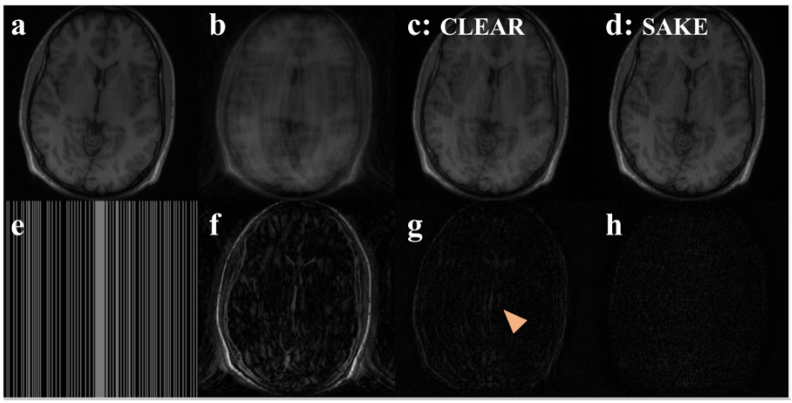

SSIM	0.7323	0.9407	0.9356
RMSE	0.0733	0.0264	0.0247

(3) Variable density sampling, R = 5

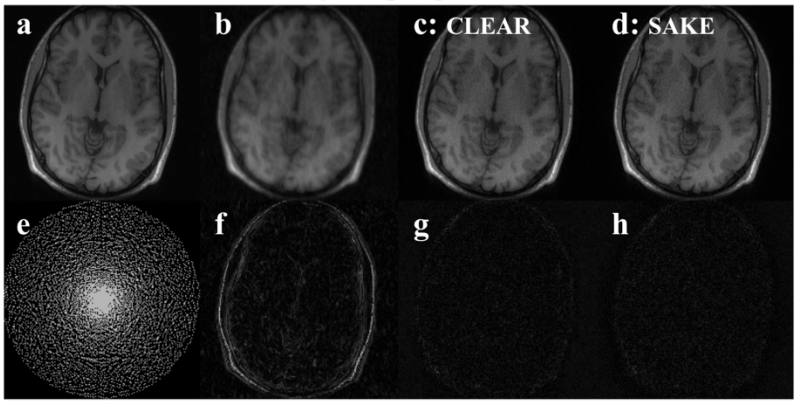

SSIM	0.8758	0.9399	0.9381
RMSE	0.0425	0.0239	0.0239

Fig 3. Reconstruction results on 1) uniform, 2) Poisson-disc and 3) variable density retrospectively under-sampled data (b) with CLEAR (c) and SAKE (d). (e) shows the sampling pattern. (f -h) show the 3 × error maps compared with the fully-sampled image (a). The table below the image shows SSIM (higher is better) and RMSE (lower is better).

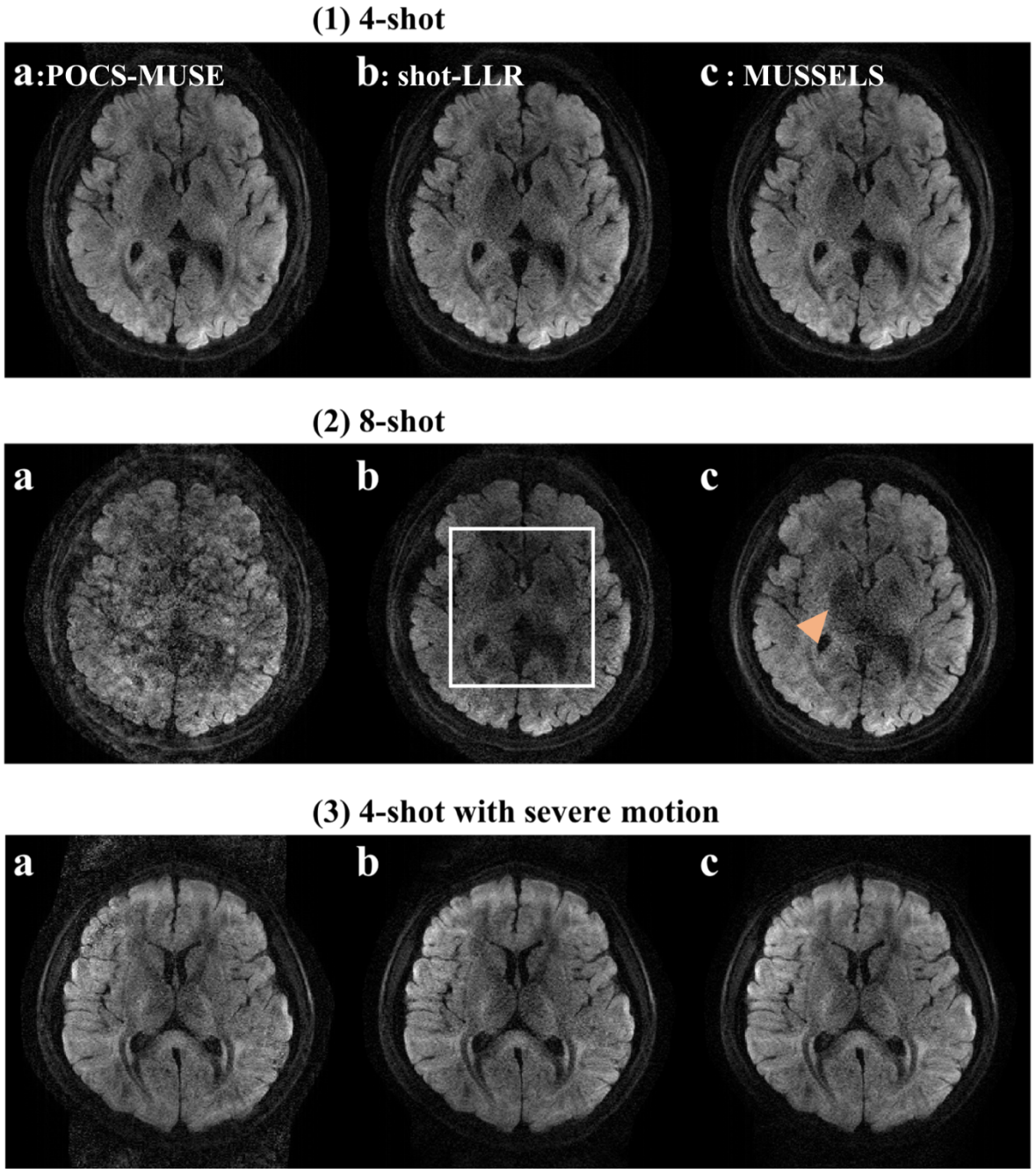

Fig 4. Multi-shot DW images reconstructed by POCS-MUSE (a), shot-LLR (b) and MUSSELS (c). In (3), the volunteer was asked to breathe deeply to simulate severe respiratory motion, and POCS-MUSE had ghosting artifacts (3a).

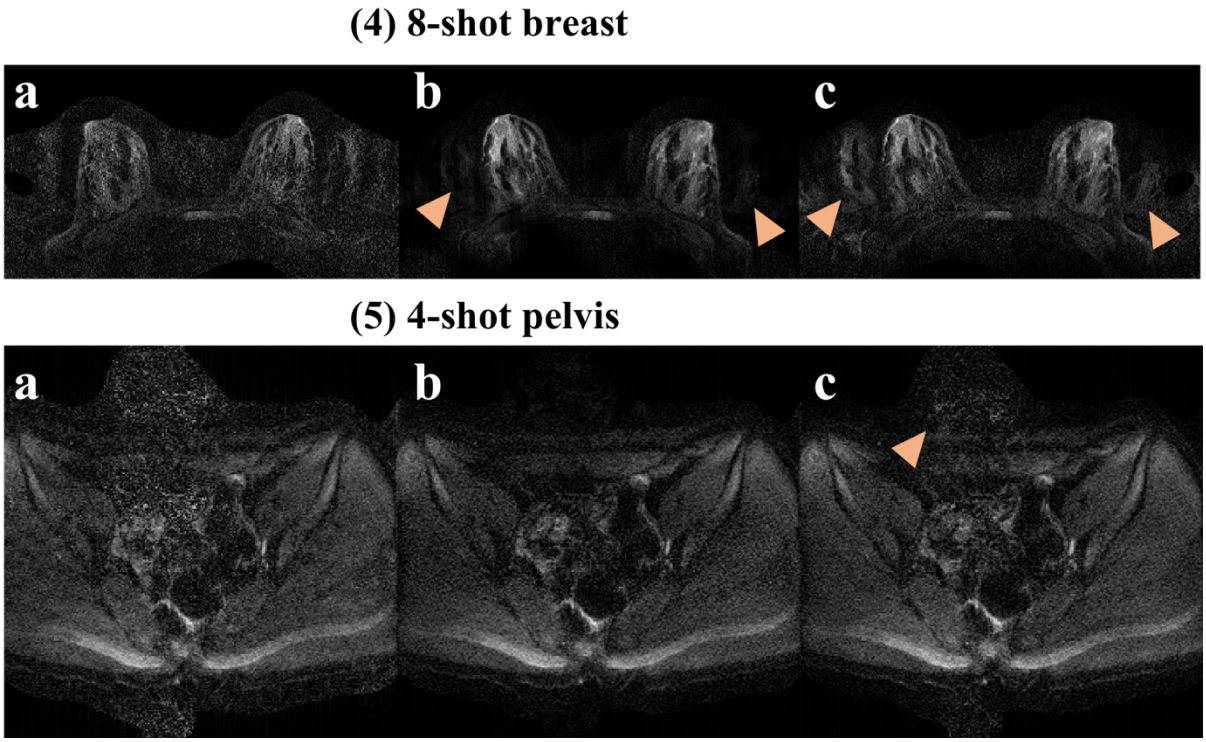

Fig 5. 8-shot breast and 4-shot pelvis images reconstructed by POCS-MUSE (a), shot-LLR (b) and MUSSELS (c). Yellow triangles pointed where the ghost artifacts were.

5. Summary

In this work, we compare two multi-shot DWI reconstruction method, shot-LLR and MUSSELS. They both outperform the conventional phase-estimation based methods and shot-LLR's motion robustness property can be very beneficial to body imaging.

It should be also noticed that these image-domain methods (CLEAR and shot-LLR) have a computational advantage compared with kspace-domain methods (SAKE and MUSSELS) since the spatial-coil/spatial-shot matrices are small and non-overlapping and computing SVD is $O(mn^2)$ for an m-by-n matrix (assuming m is big than n). This might explain why LLR is more commonly used in some other applications, e.g. dynamic image reconstruction.

References

1. Partridge SC, DeMartini WB, Kurland BF, Eby PR, White SW, Lehman CD. Differential diagnosis of mammographically and clinically occult breast lesions on diffusion-weighted MRI. J. Magn. Reson. Imaging 2010;31:562–570. doi: 10.1002/jmri.22078.

2. Moseley ME, Kucharczyk J, Mintorovitch J, Cohen Y, Kurhanewicz J, Derugin N, Asgari H, Norman D. Diffusion-weighted {MR} imaging of acute stroke: correlation with {T2}-weighted and magnetic susceptibility-enhanced {MR} imaging in cats. AJNR Am J Neuroradiol [Internet] 1990;11:423–429.

3. Basser PJ, Pajevic S, Pierpaoli C, Duda J, Aldroubi A. In vivo fiber tractography using DT-MRI data. Magn. Reson. Med. 2000;44:625–632. doi: 10.1002/1522-2594(200010)44:4<625::AID-MRM17>3.0.CO;2-O.

4. Sotiropoulos SN, Jbabdi S, Xu J, et al. Advances in diffusion MRI acquisition and processing in the Human Connectome Project. Neuroimage [Internet] 2013;80:125–143. doi: 10.1016/j.neuroimage.2013.05.057.

5. Wu W, Miller KL. Image formation in diffusion MRI: A review of recent technical developments. J. Magn. Reson. Imaging 2017:1–17. doi: 10.1002/jmri.25664.

6. Butts K, Pauly J, De Crespigny A, Moseley M. Isotropic diffusion-weighted and spiral-navigated interleaved EPI for routine imaging of acute stroke. Magn. Reson. Med. 1997;38:741–749. doi: 10.1002/mrm.1910380510.

7. Butts K, De Crespigny A, Pauly JM, Moseley M. Diffusion-weighted interleaved echo-planar imaging with a pair of orthogonal navigator echoes. Magn. Reson. Med. 1996;35:763–770. doi: 10.1002/mrm.1910350518.

8. Pipe JG, Farthing VG, Forbes KP. Multishot diffusion-weighted FSE using PROPELLER MRI. Magn. Reson. Med. 2002;47:42–52. doi: 10.1002/mrm.10014.

9. Chen N kuei, Guidon A, Chang HC, Song AW. A robust multi-shot scan strategy for high-resolution diffusion weighted MRI enabled by multiplexed sensitivity-encoding (MUSE). Neuroimage [Internet] 2013;72:41–47. doi: 10.1016/j.neuroimage.2013.01.038.

10. Chu ML, Chang HC, Chung HW, Truong TK, Bashir MR, Chen NK. POCS-based reconstruction of multiplexed sensitivity encoded MRI (POCSMUSE): A general algorithm for reducing motion-related artifacts. Magn. Reson. Med. 2015;74:1336–1348. doi: 10.1002/mrm.25527.

11. Guo H, Ma X, Zhang Z, Zhang B, Yuan C, Huang F. POCS-enhanced inherent correction of motion-induced phase errors (POCS-ICE) for high-resolution multishot diffusion MRI. Magn. Reson. Med. 2016;75:169–180. doi: 10.1002/mrm.25594.

12. Shin, Peter J., et al. "Calibrationless parallel imaging reconstruction based on structured low-rank matrix completion." Magnetic resonance in medicine 72.4 (2014): 959-970.

13. Trzasko JD, Manduca A. Calibrationless parallel MRI using CLEAR. Conf. Rec. - Asilomar Conf. Signals, Syst. Comput. 2011:75–79. doi: 10.1109/ACSSC.2011.6189958.

14. Shin, Peter J., et al. "Calibrationless parallel imaging reconstruction based on structured low-rank matrix completion." Magnetic resonance in medicine 72.4 (2014): 959-970.

15. Martin Uecker, Frank Ong, Jonathan I Tamir, Dara Bahri, Patrick Virtue, Joseph Y Cheng, Tao Zhang, and Michael Lustig, Berkeley Advanced Reconstruction Toolbox, Annual Meeting ISMRM, Toronto 2015, In Proc. Intl. Soc. Mag. Reson. Med. 23:2486

16. Uecker M, Lai P, Murphy MJ, Virtue P, Elad M, Pauly JM, Vasanawala SS, Lustig M. ESPIRiT - An eigenvalue approach to autocalibrating parallel MRI: Where SENSE meets GRAPPA. Magn. Reson. Med. 2014;71:990–1001. doi: 10.1002/mrm.24751.

17. Noll DC, Nishimura DG, Macovski A. Homodyne Detection in Magnetic Resonance Imaging. IEEE Trans. Med. Imaging 1991;10:154–163. doi: 10.1109/42.79473.